


## High-performance thermomagnetic generation in low-grade waste heat recovery

Haodong Chen(陈浩东), Hu Zhang(张虎), Mingze Liu(刘明泽), Kaiming Qiao(乔凯明), Lichen Wang(王利晨), Fengxia Hu(胡凤霞), and Baogen Shen(沈保根)
**Citation:**Chin. Phys. B, 2026, 35 (**2**): 027201. DOI: 10.1088/1674-1056/ae1205
http://cpb.iphy.ac.cn; http://iopscience.iop.org/cpb

**What follows is a list of articles you may be interested in**

---

## Realize high thermoelectric performance in both zone-melted ingots and powder-metallurgy bulks of Bi0.46Sb1.54Te3

Kai-Wen Zhao(赵凯雯), Meng-Yao Li(李梦瑶), Ying-Jiu Zhang(张迎九), and Hong-Zhang Song(宋红章)
Chin. Phys. B, 2025, 34 (**10**): 107203. DOI: 10.1088/1674-1056/add503

## High-entropy alloys in thermoelectric application: A selective review

Kai Ren(任凯), Wenyi Huo(霍文燚), Shuai Chen(陈帅), Yuan Cheng(程渊), Biao Wang(王彪), and Gang Zhang(张刚)
Chin. Phys. B, 2024, 33 (**5**): 057202. DOI: 10.1088/1674-1056/ad34c5

## Rational design and synthesis of Cr1-xTe/Ag2Te composites for solid-state thermoelectromagnetic cooling near room temperature

Xiaochen Sun(孙笑晨), Chenghao Xie(谢承昊), Sihan Chen(陈思汗), Jingwei Wan(万京伟), Gangjian Tan(谭刚健), and Xinfeng Tang(唐新峰)
Chin. Phys. B, 2024, 33 (**5**): 057201. DOI: 10.1088/1674-1056/ad2d57

## Ga intercalation in van der Waals layers for advancing p-type Bi2Te3-based thermoelectrics

Yiyuan Chen(陈艺源), Qing Shi(石青), Yan Zhong(钟艳), Ruiheng Li(李瑞恒), Liwei Lin(林黎蔚), Ding Ren(任丁), Bo Liu(刘波), and Ran Ang(昂然)
Chin. Phys. B, 2023, 32 (**6**): 067201. DOI: 10.1088/1674-1056/acc2af

## Advancing thermoelectrics by suppressing deep-level defects in Pb-doped AgCrSe2 alloys

Yadong Wang(王亚东), Fujie Zhang(张富界), Xuri Rao(饶旭日), Haoran Feng(冯皓然), Liwei Lin(林黎蔚), Ding Ren(任丁), Bo Liu(刘波), and Ran Ang(昂然)
Chin. Phys. B, 2023, 32 (**4**): 047202. DOI: 10.1088/1674-1056/acb765

---

**TOPICAL REVIEW — Multiferroicity and multicaloric effects**

# High-performance thermomagnetic generation in low-grade waste heat recovery

Haodong Chen(陈浩东)[1], Hu Zhang(张虎)[1,†], Mingze Liu(刘明泽)[1], Kaiming Qiao(乔凯明)[1], Lichen Wang(王利晨)[2], Fengxia Hu(胡凤霞)[3,‡], and Baogen Shen(沈保根)[2,3,§]

[1] *School of Materials Science and Engineering, University of Science and Technology of Beijing, Beijing* 100083, *China*
[2] *Ningbo Institute of Materials Technology and Engineering, Chinese Academy of Sciences, Ningbo* 315201, *China*
[3] *Beijing National Laboratory for Condensed Matter Physics, Institute of Physics, Chinese Academy of Sciences, Beijing* 100190, *China*

(Received 2 September 2025; revised manuscript received 10 October 2025; accepted manuscript online 11 October 2025)

Thermomagnetic generation (TMG), a heat-to-electricity conversion technology based on the thermomagnetic effect, offers high reliability and broad adaptability to diverse heat sources. By exploiting the temperature-dependent magnetization of thermomagnetic materials, TMG converts thermal energy into electrical energy through cyclic changes in magnetic flux based on Faraday's law. The performance of TMG systems is largely governed by the intrinsic properties of the working materials and the design of device architecture. Ideal TMG materials exhibit sharp and reversible magnetization transitions near the operating temperature, low thermal hysteresis, and high thermal conductivity. Device configurations can be broadly categorized into active and passive systems: active TMG devices rely on controlled thermal cycling and optimized magnetic circuits for enhanced output, whereas passive devices utilize self-actuated mechanical motion to generate electricity. In this topical review, we provide a comprehensive overview of recent advances in TMG materials and device configurations. Furthermore, we discuss future development trends and offer perspectives on experimental strategies to advance this field.

**Keywords:** low grade waste heat, thermal energy recovery, thermomagnetic generation

**PACS:** 72.15.Jf, 75.30.Kz, 77.65.–J

**DOI:** 10.1088/1674-1056/ae1205 **CSTR:** 32038.14.CPB.ae1205

## 1. Introduction

Waste heat, an inevitable byproduct of energy conversion processes governed by the second law of thermodynamics, exists in various forms and temperatures.[1,2] While high- and medium-grade waste heats (above 230 °C) can be efficiently recovered due to their concentrated sources and higher thermodynamic efficiency, low-grade waste heat (below 230 °C) is often underutilized because of its dispersed distribution and limited conversion efficiency.[3,4] However, low-grade waste heat accounts for over 60% of the total recoverable thermal energy and offers significant potential for energy savings and carbon emission reduction.[5,6] Therefore, despite existing technical challenges, the efficient recovery and utilization of low-grade waste heat is essential for meeting growing energy demands and promoting sustainable energy systems.

Over the past few decades, considerable efforts have been devoted to developing alternative technologies for harvesting low-grade waste heat. Current approaches are primarily based on thermoelectric,[7–9] pyroelectric,[10–13] and thermomagnetic[14,15] effects. Among them, thermoelectric generators (TEGs), which operate via the Seebeck effect, are the most extensively studied. However, TEGs typically require a large temperature gradient to achieve meaningful power output, and their energy efficiency drops significantly when the heat source temperature falls below 200 °C, limiting their effectiveness for low-grade waste heat recovery.[16] Pyroelectric generators (PEGs) generate current by cyclically exposing the material to hot and cold environments. Despite their fast response and high conversion efficiency at the device level, their low output current, high internal impedance, and limited power density restrict their use in large-scale applications.[17] The Organic Rankine Cycle (ORC) can achieve relatively high efficiency in low-temperature ranges, but its reliance on organic working fluids raises environmental concerns due to potential emissions.[18] Additionally, liquid-state energy harvesting techniques from low-enthalpy sources, such as thermomagnetic hydrodynamic systems,[19] pyroelectric microgenerators,[20] and triboelectric harvesters,[21,22] have shown promise in powering microsystems and wearable electronics. Nonetheless, issues such as nanoparticle deposition in magnetic fluids and difficulties in liquid control continue to hinder their practical implementation.[19,21]

A fundamentally different approach to thermal-to-

†Corresponding author. E-mail: zhanghu@ustb.edu.cn
‡Corresponding author. E-mail: fxhu@iphy.ac.cn
§Corresponding author. E-mail: shenbg@iphy.ac.cn

© 2026 Chinese Physical Society and IOP Publishing Ltd. All rights, including for text and data mining, AI training, and similar technologies, are reserved.

electrical energy conversion is thermomagnetic generation (TMG), which directly exploits the thermomagnetic effect, that is, the strong temperature dependence of magnetization in ferromagnetic materials undergoing sharp phase transitions near their transition temperature. In the late 19th century, Tesla and Edison described early TMG concepts for converting heat into mechanical or electrical energy.[23,24] However, early materials such as iron (Fe) proved impractical for waste heat recovery due to their high Curie temperature ($T_C$) and low conversion efficiency.[25,26] Later, Kirol and Mills conducted numerical analyses of regenerative TMG systems using Fe, $Ho_{69}Fe_{31}$, and Gd as working materials.[27] Although Fe and $Ho_{69}Fe_{31}$ demonstrated higher theoretical power densities than Gd, their $T_C$ (1043 K and 77 K, respectively) rendered them unsuitable for practical applications. Gadolinium ($T_C = 292$ K), with a more appropriate operating temperature near room temperature, became the most viable TMG candidate, despite its relatively low power density. These limitations stalled further exploration of TMG for several decades. In recent years, interest in TMG has re-emerged, driven by advances in high-performance magnetic materials and improved exploration of thermal transport interfaces. Notably, the requirements for TMG materials largely overlap with those of magnetocaloric effect (MCE) materials,[28–30] leading to renewed focus on MCE systems as potential TMG candidates.[31–33] In 2011, Srivastava *et al.*[34] demonstrated that the multiferroic Heusler alloy $Ni_{45}Co_5Mn_{40}Sn_{10}$, which undergoes a first-order magnetic transition (FOMT) from ferromagnetic (FM) austenite to weakly magnetic martensite, exhibited promising TMG properties. More recently, typical MCE materials such as Gd, $Gd_5(Si, Ge)_4$, NiMn-based Heusler alloys, and $La(Fe, Si)_{13}H_y$/In composites have been reported to possess strong potential for TMG applications.[31] Nevertheless, identifying materials that combine high TMG performance with compatibility for low-grade waste heat harvesting remains a significant challenge.

TMG devices can generally be categorized into active and passive types based on their energy conversion mechanisms. Active devices rely on externally controlled thermal cycling and engineered magnetic circuits to directly convert heat into electricity through magnetic flux changes, offering stable and continuous output suitable for system-level integration. These devices typically feature optimized coil designs, magnetic shielding, and thermal interfaces to enhance performance. In contrast, passive TMG devices utilize thermally induced mechanical motion, such as in thermomagnetic oscillators and Curie wheels, where motion is driven by periodic magnetic phase transitions under thermal gradients. These systems are self-actuated and advantageous for low-maintenance or remote scenarios. However, both types face challenges: active devices often suffer from inefficient heat transfer and scaling limitations, while passive systems struggle to maintain stable mechanical motion under variable conditions. Overcoming these limitations will require not only improved materials but also advancements in thermal management, magnetic circuit design, and hybrid integration strategies.

In this review, we highlight our recent progress in TMG research and provide a comprehensive summary of advancements from both materials and device perspectives. We discuss key material properties such as phase transition behavior, magnetization change, and thermal stability, as well as the evolution of device architectures from early designs to integrated systems. Finally, we outline current challenges and future directions to guide the development of high-performance TMG materials and scalable device solutions for efficient low-grade heat recovery.

## 2. The thermomagnetic cycle for harvesting waste heat

As the foundation of TMG, the thermomagnetic cycle defines how magnetic and thermal energy interact to produce electrical output. Figure 1(a) illustrates an ideal thermomagnetic cycle consisting of four steps. In step I, the TMG material is initially at ambient temperature, below its $T_C$, and exhibits a high magnetization ($M_{cold}$). At this stage, a magnetic field ($H$) is applied isothermally, reducing the Gibbs energy of the material. In step II, low-grade waste heat ($Q_{in}$) is used to raise the material's temperature above $T_C$, leading to a sharp decrease in magnetization to $M_{hot}$. In step III, the magnetic field is removed, and only a small amount of Gibbs energy is required to maintain the system. In step IV, the hot material is cooled back to ambient temperature, completing the cycle and restoring $M_{cold}$. During the cycle, the change in Gibbs energy, expressed as $\mu\Delta MH$, is harnessed to generate electrical energy, where $\mu$ is the magnetic permeability of free space and $\Delta M = M_{cold} - M_{hot}$ is the magnetization difference that determines the energy conversion capability.[35]

Figure 1(b) shows the schematic view of a proposed TMG device. The TMG material is positioned above a permanent magnet that provides a background magnetic field and is surrounded by a pickup coil. When the material undergoes periodic heating and cooling, its magnetization changes due to thermally induced magnetic transitions between ferromagnetic (FM) and paramagnetic (PM) states. This variation alters the magnetic flux through the coil, and, according to Faraday's law, an alternating current (AC) is continuously generated in the coil. This mechanism enables the direct conversion of thermal energy into electrical energy without any moving parts. As a result, thermomagnetic generation offers a promising approach for efficient and reliable harvesting of low-grade waste heat.[36]

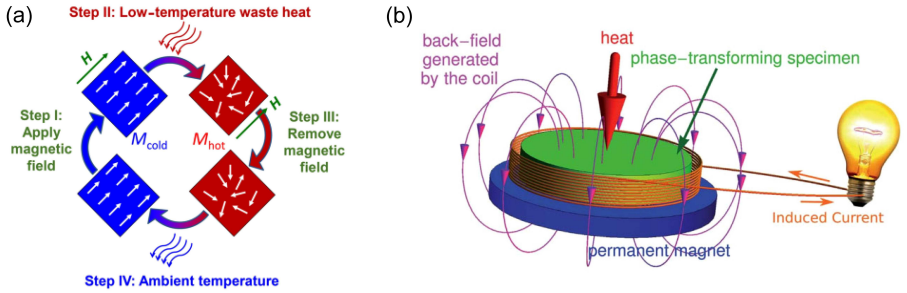



**Fig. 1.** (a) A TMG material is subjected to four steps within a thermomagnetic cycle.[35] (b) A schematic view of the proposed TMG device.[36]

## 3. Soft magnetic materials for TMG

### 3.1. Key performance metrics of TMG materials

#### 3.1.1. Magnetization change ($\mathrm{d}M/\mathrm{d}T$) and temperature change ($\mathrm{d}T/\mathrm{d}t$)

According to Faraday's law, the induced current ($I$) in the coil can be expressed as[37,38]

$$I = \frac{E}{R} = -\frac{NS}{R}\frac{\mathrm{d}B}{\mathrm{d}t}, \tag{1}$$

where $E$ is the electrodynamic potential, $N$ is the number of coil turns, $S$ is the cross-section area of the coil, and $\mathrm{d}B/\mathrm{d}t$ is the change rate of magnetic flux. For a given TMG device, the product $NS$ is constant and independent of the material. Therefore, the induced current depends on $\mathrm{d}B/\mathrm{d}t$, which in turn is influenced by the magnetization change rate $\mathrm{d}M/\mathrm{d}t$ (since $B = \mu_0(H+M)$).[39,40] This rate can be further decomposed as $(\mathrm{d}M/\mathrm{d}T)(\mathrm{d}T/\mathrm{d}t)$. Hence, superior TMG performance requires both a large magnetization gradient $(\mathrm{d}M/\mathrm{d}T)$ and a rapid temperature response $(\mathrm{d}T/\mathrm{d}t)$.

#### 3.1.2. Energy conversion efficiency

The relative energy conversion efficiency ($\eta_{\mathrm{rel}}$) characterizes the capacity of TMG materials to convert thermal energy into electrical energy during one thermomagnetic cycle, and is defined as[18,35]

$$\eta_{\mathrm{rel}} = \frac{\eta_{\mathrm{abs}}}{\eta_{\mathrm{Carnot}}} = \frac{\eta_{\mathrm{abs}}}{T_{\mathrm{hot}} - T_{\mathrm{cold}}} T_{\mathrm{hot}}, \tag{2}$$

where $\eta_{\mathrm{Carnot}}$ is the theoretical Carnot efficiency, $T_{\mathrm{hot}}$ and $T_{\mathrm{cold}}$ are the temperatures of hot and cold ends, respectively. The absolute efficiency ($\eta_{\mathrm{abs}}$) is given by[17,35,39]

$$\eta_{\mathrm{abs}} = \frac{E_{\mathrm{out}}}{Q_{\mathrm{in}}}, \tag{3}$$

where $E_{\mathrm{out}}$ represents the net magnetic energy output. Assuming energy is gained by the voltage source, the output energy can be written as[17,35,39]

$$E_{\mathrm{out}} = -\mu_0 H \Delta M. \tag{4}$$

The thermal energy input ($Q_{\mathrm{in}}$) is determined by integrating the heat capacity over the working temperature range:[39]

$$Q_{\mathrm{in}} = \rho \int_{T_{\mathrm{cold}}}^{T_{\mathrm{hot}}} C_P(T)\,\mathrm{d}T, \tag{5}$$

where $C_P(T)$ is the specific heat of the material. Therefore, to improve thermodynamic efficiency, materials should exhibit both a high $\Delta M$ and a low $Q_{\mathrm{in}}$.

#### 3.1.3. Power density and cost index

The average power density ($P_{\mathrm{D-ave}}$) measures the electrical power output per unit volume and is calculated as follows:[41]

$$P_{\mathrm{D-ave}} = \frac{\int_0^t V^2(t)\,\mathrm{d}t}{RV_{\mathrm{vol}}t}, \tag{6}$$

where $V(t)$ is the time-dependent output voltage, $R$ is the total system resistance, and $V_{\mathrm{vol}}$ is the volume of the material. The maximum power density ($P_{\mathrm{D-max}}$) refers to the peak output power per unit volume and is given by[42,43]

$$P_{\mathrm{D-max}} = \frac{E_{\mathrm{max}}^2}{RV_{\mathrm{vol}}}, \tag{7}$$

where $E_{\mathrm{max}}$ is the maximum induced voltage during a cycle. To assess cost performance, the cost index ($C$) is introduced and defined as[31,35,44,45]

$$C_0 = \frac{C}{P_{\mathrm{D-max}}}, \tag{8}$$

where $C$ represents the cost of the raw material per unit. This index gives the price in euros required for each Watt of output power and reflects the economic efficiency of TMG materials.

#### 3.1.4. Power generation index

Beyond the metrics above, a power generation index (PGI) has been proposed to enable more systematic comparison among TMG materials. It is calculated as[44,45]

$$\mathrm{PGI} = \frac{I_0}{\Delta T \cdot R \cdot H \cdot \omega}, \tag{9}$$

where $I_0$ is the experimental induced current density, $\Delta T$ is the temperature span, $R$ is the system resistance, $H$ is the applied magnetic field, and $\omega$ is the number of coil turns. This metric incorporates both material and device-level parameters influencing current generation. As such, PGI minimizes the influence of non-intrinsic variables and enables a more objective evaluation of TMG performance across different materials.

### 3.2. Traditional TMG materials and their characteristics

The selection of a suitable TMG material has a significant impact on the overall performance of a TMG system. For optimal operation, TMG materials should exhibit a combination of favorable thermal and magnetic properties: First, soft magnetic behavior with low remanent magnetization ($M_r$) is preferred to facilitate rapid magnetic reversibility during thermal cycling. Second, the material should possess a tunable $T_C$, ideally within the range suitable for low-grade heat sources. Third, a sharp and reversible magnetization change near $T_C$ is essential to maximize the magnetic flux variation and enhance energy conversion efficiency. Additionally, high thermal conductivity is required to ensure fast heat transfer and enable rapid temperature changes. Finally, low cost and material availability are also important considerations for practical and scalable TMG applications.

Gadolinium is one of the most widely studied TMG materials for thermal energy harvesting,[40,46–48] primarily for two reasons. First, it possesses a $T_C$ of $\sim 292$ K,[49] making it suitable for operation near room temperature. Second, Gd undergoes a second-order magnetic transition (SOMT) from the FM to the PM state and exhibits negligible thermal and magnetic hysteresis, which is advantageous for cyclic operation. However, since Gd becomes paramagnetic at room temperature, it typically requires a heat sink or refrigeration system to maintain thermal cycling. In practical applications, heat sources, especially in the form of industrial waste heat, are more accessible than effective heat sinks. Therefore, TMG materials with a $T_C$ slightly above room temperature are practically preferred. As an alternative to Gd, Srivastava *et al.*[34] recently proposed a multiferroic Heusler alloy, $Ni_{45}Co_5Mn_{40}Sn_{10}$, which undergoes a FOMT from a strongly FM austenite phase to a weakly FM martensite phase at a critical temperature of 408 K.[36,50] Although the work output per TMG cycle is higher for Heusler alloys than for Gd, both materials exhibit comparable efficiency. This is because the energy requirement at the transition temperature differs: FOMT is dominated by latent heat, while SOMT is governed primarily by sensible heat.[51] As a result, Heusler alloys require a greater heat input per cycle compared to Gd.

In addition to Gd and NiMn-based Heusler alloys, a wide range of alternative thermomagnetic materials have been reported, including Gd-based compounds,[31,52,53] (Mn, Fe)$_2$(P, $X$) ($X$ = As, Si) alloys,[54–56] $MM'X$ ($M, M'$ = transition metals, $X$ = carbon or boron group elements) alloys,[14,33] FeNi alloys,[57,58] and LaFe-based compounds.[32,43,59] Most of these materials exhibit FOMT, which are associated with large entropy and magnetization changes, features that are beneficial for TMG applications. However, FOMT materials often suffer from thermal/magnetic hysteresis, structural instability, or high heat input requirements due to latent heat, all of which can reduce long-term efficiency and device reliability. Hence, trade-offs between material performance (e.g., sharp magnetization change), thermal properties (e.g., conductivity and specific heat), and economic factors (e.g., rare earth content and cost) must be carefully considered in future material screening and device design.

### 3.3. Experimental evaluation of classic magnetocaloric materials

Based on the same active TMG device, Chen *et al.*[31] evaluated the TMG performance of several classic magnetocaloric materials, such as Gd, $Gd_5(Si, Ge)_4$, NiMn-based Heusler alloy, and La(Fe, Si)$_{13}$H$_y$/In materials, and all materials were tested under identical experimental conditions for fair comparison. Figure 2(a) shows their $M$–$T$ curves under 1 T magnetic field. All samples undergo a magnetic transition from the FM to PM state during heating, and the reverse transition from the PM to FM state during cooling. None of the samples exhibit thermal hysteresis, confirming their SOMT nature. The inset of Fig. 2(a) shows the corresponding $\mathrm{d}M/\mathrm{d}T$–$T$ curves, the $T_C$ of Gd, $Gd_5(Si, Ge)_4$, NiMn-based Heusler alloy, and La(Fe, Si)$_{13}$H$_y$/In composite is 292 K, 302 K, 322 K, and 340 K. For all samples, the magnetic transitions occurred within the working temperature range of the TMG device, enabling a direct evaluation of their TMG performance under relevant operating conditions.

Figure 2(b) shows the average temperature variation with time during one TMG cycle. For all samples, both heating and cooling rates are initially rapid within the first 2 s due to the large temperature gradient between the sample and the heating/cooling water. As the temperature difference decreases, the rates gradually slow down. The inset of Fig. 2(b) shows the corresponding $\mathrm{d}T/\mathrm{d}t$ curves derived from the $T$–$t$ curves, where the La(Fe, Si)$_{13}$H$_y$/In composite exhibits the highest $\mathrm{d}T/\mathrm{d}t$, a desirable feature for superior TMG performance. Moreover, since the $T_C$ of the La(Fe, Si)$_{13}$H$_y$/In composite (340 K) is closer to the hot end temperature (353 K), its magnetic transition occurs earlier during cooling, leading to a larger $\mathrm{d}T/\mathrm{d}t$ around $T_C$ compared to the heating cycle. This implies that the relative position of $T_C$ within the working temperature span largely affects $\mathrm{d}T/\mathrm{d}t$, which would then affect the induced current $I$ according to Faraday's law. Therefore, the location of $T_C$ within the working temperature range would complicate the direct TMG performance comparisons among materials with different $T_C$ values.

To eliminate the influence of extrinsic thermal conditions, the temperature ranges were hypothetically adjusted so that the $T_C$ of all samples were positioned similarly within the thermal cycle. Figure 2(c) shows the $\mathrm{d}M/\mathrm{d}t$–$t$ curves before and after shifting the temperature span. The maximum $\mathrm{d}M/\mathrm{d}t$ occurs at the onset of each cycle. After alignment, the maximum $\mathrm{d}M/\mathrm{d}t$ during heating remains nearly unchanged for

$Gd_5(Si, Ge)_4$ and the NiMn-based Heusler alloy, but increases significantly for the La(Fe, $Si)_{13}H_y$/In composite, indicating improved TMG performance. The intrinsic TMG performance and energy conversion efficiency of the tested materials were fairly evaluated. Figure 2(d) compares the key factors for all the materials tested. Gd exhibits the highest conversion efficiency (1.46%) due to its combination of large magnetization change and relatively low heat input. Meanwhile, the La(Fe, $Si)_{13}H_y$/In composite generates the highest induced current (9.12 $\mu A \cdot g^{-1}$) and power density (0.47 $mW \cdot m^{-3}$). Notably, its cost index is 1–2 orders of magnitude higher than that of other candidates, underscoring its potential as a cost-effective and high-performance TMG candidate for low-grade waste heat recovery.

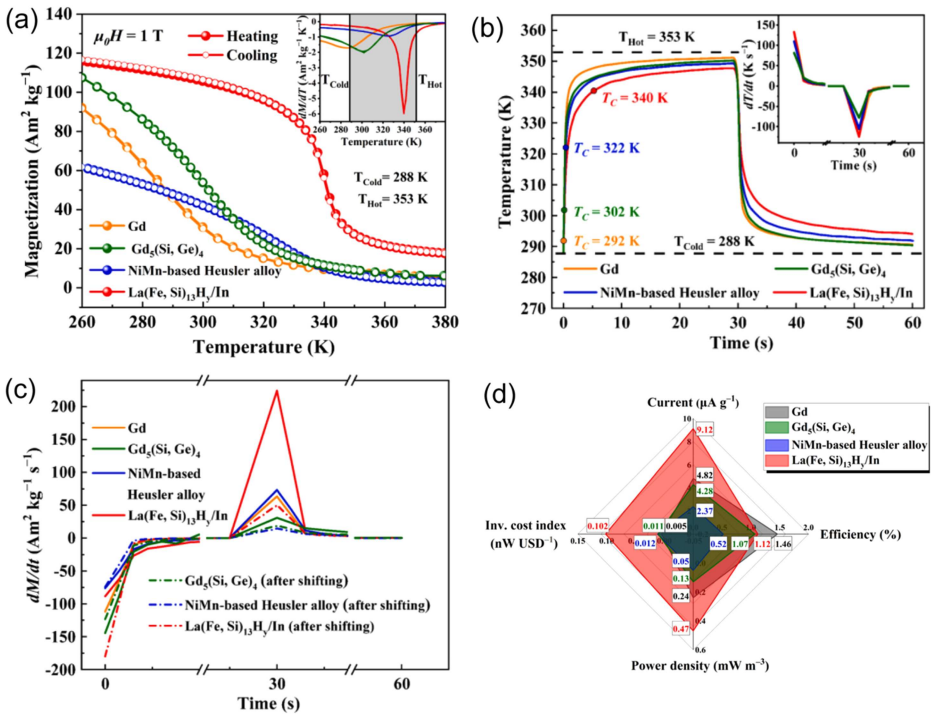



**Fig. 2.** (a) The $M$–$T$ curves under 1 T field for Gd, $Gd_5(Si, Ge)_4$, NiMn-based Heusler alloy, and La(Fe, $Si)_{13}H_y$/In composite. The inset shows the corresponding $dM/dT$–$T$ curves. (b) The $T$–$t$ curves for all the samples. The inset shows the corresponding $dT/dt$–$t$ curves. (c) The $dM/dt$–$t$ curves before and after shifting the temperature span. (d) Evaluation of key TMG properties for all the samples.[31]

### 3.4. Comparison of first-order and second-order transition materials

To investigate the influence of different phase transitions on TMG performance, Chen *et al.*[45] systematically compared three Heusler alloys with similar composition but distinct transition types using a lab-built active TMG device. Figure 3(a) presents the $M$–$T$ curves of $Ni_{37.5}Co_{12.5}Mn_{35}Ti_{15}$ (Co12.5), $Ni_{36}Co_{14}Mn_{35.7}Ti_{14.3}$ (Co14), and $Ni_2Mn_{1.4}In_{0.6}$ (NiMnIn) under a 1 T magnetic field. For Co12.5, both FOMT and SOMT occur within the working temperature range, whereas only the FOMT in Co14 and the SOMT in NiMnIn are active under working conditions. The presence of thermal hysteresis ($\sim$ 20 K) in FOMT would lead to notable asymmetry in TMG performance during heating and cooling, necessitating a wide temperature span to encompass both transitions during cycling. In contrast, NiMnIn exhibits a fully reversible SOMT within the operating range, free of thermal hysteresis, resulting in a consistent peak $dM/dT$ value of 1.78 $A \cdot m^2 \cdot kg^{-1} \cdot K^{-1}$ during both heating and cooling. Moreover, the parent phase of NiMnIn shows a higher magnetization (90.8 $A \cdot m^2 \cdot kg^{-1}$) than those of Co12.5 and Co14, leading to a greater magnetization change ($\Delta M$) across the transition. This larger $\Delta M$ supports more effective energy conversion during the phase transition, thereby benefiting the overall TMG performance.

Figure 3(b) shows the experimental and simulated voltage in one cycle. All samples exhibit stable AC voltage output under continuous TMG operation. The simulated $V$–$t$ curves align well with the experimental results, confirming the reliability of the experimental TMG performance. Positive voltage is induced during increasing magnetization, while negative voltage appears during decreasing magnetization. Notably, Co12.5 and Co14 produce a large positive voltage peak (points a, c) followed by a smaller negative peak (points b, d) in each cycle, consistent with successive FOMT and SOMT transitions. In contrast, NiMnIn produces a single voltage peak per heating or cooling half-cycle, reflecting its single, continuous SOMT.

Figure 3(c) compares the key performance metrics of the three alloys. Benefiting from its favorable thermal properties and high $dM/dt$, NiMnIn achieves the highest $V_{max}$ (1.92 $mV \cdot g^{-1}$). Although Co12.5 and Co14 produce four voltage peaks per cycle, the total voltage output ($V_{tol}$) over

300 s for NiMnIn (2.68 V) matches or exceeds that of Co12.5 (1.82 V) and Co14 (2.68 V). Additionally, NiMnIn outperforms Co12.5 and Co14 in terms of relative efficiency $\eta_{\rm rel}$ ($1.09\times10^{-4}$%), power density $P_{\rm D-ave}$ (0.5 μW·cm$^{-3}$), and cost index $C$ (2.78 μW per €). Notably, its maximum power density $P_{\rm D-max}$ (1752.3 mW·m$^{-3}$) and cost index are 1–5 and 1–4 orders of magnitude higher, respectively, than those of most typical TMG candidates reported.

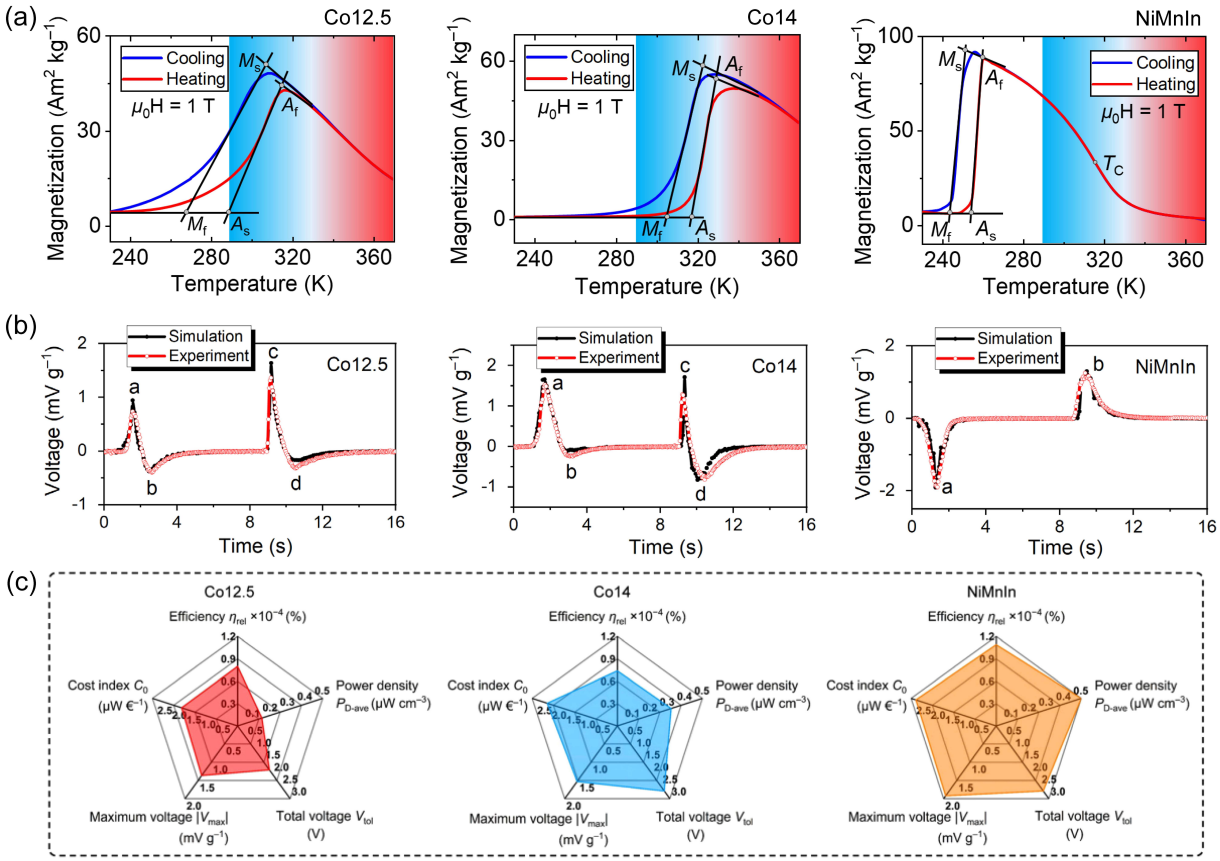



**Fig. 3.** (a) The $M$–$T$ curves of the alloys under 1 T field. (b) The experimental and simulated $V$–$t$ curves in one cycle. (c) Comprehensive evaluation of key properties for all three alloys.[45]

In addition to its high energy output, NiMnIn also exhibits exceptional operational durability. While typical FOMT materials often suffer from structural fatigue and performance degradation within minutes, NiMnIn remains stable under continuous cycling for over a month. These results highlight a promising shift from traditional FOMT materials to SOMT systems. Consequently, the favorable combination of high power output, zero hysteresis, and long-term reliability positions SOMT Heusler alloys like NiMnIn as more practical and reliable candidates for future TMG applications.

### 3.5. Enhanced heat transfer property for TMG materials

Ideal TMG materials are expected to exhibit not only a sharp magnetization change $\mathrm{d}M/\mathrm{d}T$ but also a rapid temperature response $\mathrm{d}T/\mathrm{d}t$ near the $T_C$. However, most reported materials suffer from low $\mathrm{d}T/\mathrm{d}t$ due to their inherently low thermal conductivity ($\lambda$).[31,45,49] To address this issue, low-melting-point indium (In), which possesses a high thermal conductivity of 82 W·m$^{-1}$·K$^{-1}$, was introduced into a typical Ni–Mn–In alloy to form Ni–Mn–In/In composites.[44] Figure 4(a) illustrates the schematic fabrication process of Ni–Mn–In/In composites. The annealed bulk Ni–Mn–In ingot was first ground and sieved into powders. These powders were then mixed with In powders in varying weight fractions ranging from 20 wt.% to 90 wt.% (denoted as In20–In90). The resulting powder mixtures were consolidated into cylindrical pellets (Φ10 mm) via hot pressing. Since the hot pressing temperature (403–413 K) is close to the melting point of In (430 K), In metal enters a semi-molten state with high fluidity, enabling it to infiltrate the interparticle pores between Ni–Mn–In grains and enhance the structural densification of the composite.

Figure 4(b) shows the thermal diffusivity ($\alpha$) of In20−In90 composites and Ni–Mn–In alloy. The $\alpha$ of the composites increases significantly with increasing In content, from $0.45\times10^{-5}$ m$^2$·s$^{-1}$ for In20 to $3.45\times10^{-5}$ m$^2$·s$^{-1}$ for In90. This is notably higher than that of pure Ni–Mn–In ($0.28\times10^{-5}$ m$^2$·s$^{-1}$), indicating that the composite responds more quickly to ambient temperature changes. As shown in the inset of Fig. 4(b), a higher $\alpha$ facilitates more rapid heat propagation within the material, leading to an increased temperature variation rate ($\mathrm{d}T/\mathrm{d}t$), which in turn induces a larger voltage output according to Faraday's law.

Geometric optimization further improves performance: by reducing thickness to 2 mm and introducing 7 holes into the In40 composite. Figure 4(c) compares the key performance metrics between the Ni–Mn–In bulk and the In40 composite (2 mm, 7 holes), and the inset shows the morphology of the two samples. The In40 composite demonstrates enhanced TMG performance across all evaluated parameters. Specifically, its $P_{D-ave}$ reaches 0.046 $\mu W \cdot g^{-1}$ and $P_{D-max}$ reaches 0.433 $\mu W \cdot g^{-1}$, representing 1.8 and 2.4 times improvements, respectively, over the Ni–Mn–In bulk. Additionally, this optimized In40 composite achieves a thermal conductivity 15 times higher and a PGI 8 orders of magnitude greater than those of other reported TMG materials, as shown in Fig. 4(d). The combination of significantly improved heat transfer and favorable properties, such as zero thermal hysteresis, good machinability, corrosion resistance, and long-term cycling stability, positions the Ni–Mn–In/In composite as a highly promising material for low-grade waste heat recovery.

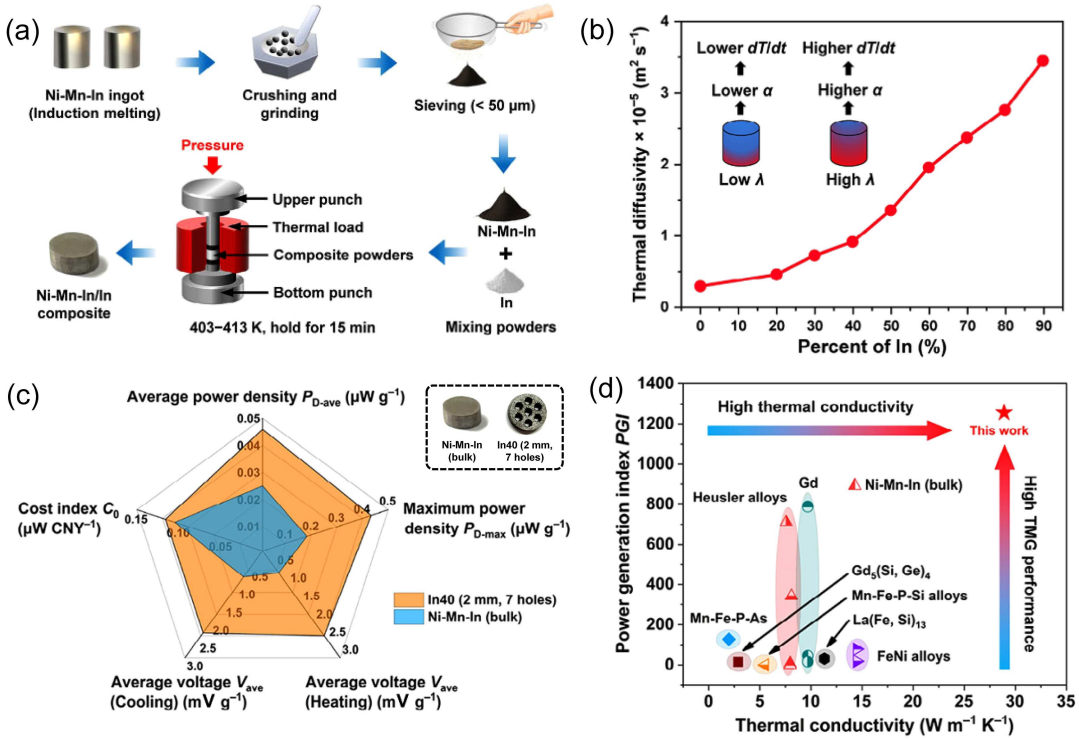



**Fig. 4.** (a) Schematic illustration of the hot pressing process to fabricate Ni–Mn–In/In composites. (b) Thermal diffusivity ($\alpha$) of In20–In90 composites and Ni–Mn–In alloy. The inset shows the relationship between $\alpha$ and $dT/dt$. (c) Evaluation of key TMG properties for Ni–Mn–In and the In40 composite (2 mm, 7 holes). The inset shows the morphology of the two samples. (d) Comparison of the PGI and $\lambda$ of the In40 composite (2 mm, 7 holes) with those materials used in active TMG devices with traditional magnetic circuits.[44]

### 3.6. Theoretical comparison of classic magnetocaloric materials

Figures 5(a) and 5(b) present Ashby-type plots showing the energy conversion efficiency ($\eta$) of various TMG materials as a function of magnetization change ($\Delta M$) and heat input ($Q_{in}$). Only materials with $T_C$ between 273 K and 373 K were considered. The performance was evaluated under two different temperature gradients ($\Delta T$) of 10 K and 30 K. The most efficient materials appear in the upper-left region of the plots, where $\eta$ approaches 2%. At $\Delta T = 10$ K (Fig. 5(a)), materials undergoing a first-order magnetic transition (represented by half-solid symbols) exhibit the highest efficiencies, owing to their sharp magnetization change within a narrow temperature range. In contrast, at $\Delta T = 30$ K (Fig. 5(b)), second-order transition materials (solid symbols) tend to perform better, benefiting from a broader transition. Among all candidates, Gd-based materials demonstrate consistently high efficiency across both $\Delta T$ conditions, especially under low heat input. Notably, the $Gd_5(SiGe)_4$, originally developed as a magnetocaloric material, achieves the highest efficiency at $\Delta T = 10$ K.[35]

However, magnetocaloric materials typically have high specific heat, which is unfavorable for TMG applications due to increased thermal losses. To achieve high-efficiency TMG, new material systems that combine low specific heat with large $\Delta M$ and reversible transitions are needed.[16] It is also worth noting that, despite promising theoretical predictions, the experimentally measured efficiencies of current TMG devices remain significantly lower. This discrepancy arises primarily from non-ideal heat transfer, magnetic flux leakage, thermal hysteresis, and parasitic losses in actual devices. Future efforts should focus on optimizing both materials and system design, including enhancing thermal transport, minimizing energy dissipation, and improving magnetic circuit topology, to narrow the gap between theoretical and practical efficiency.

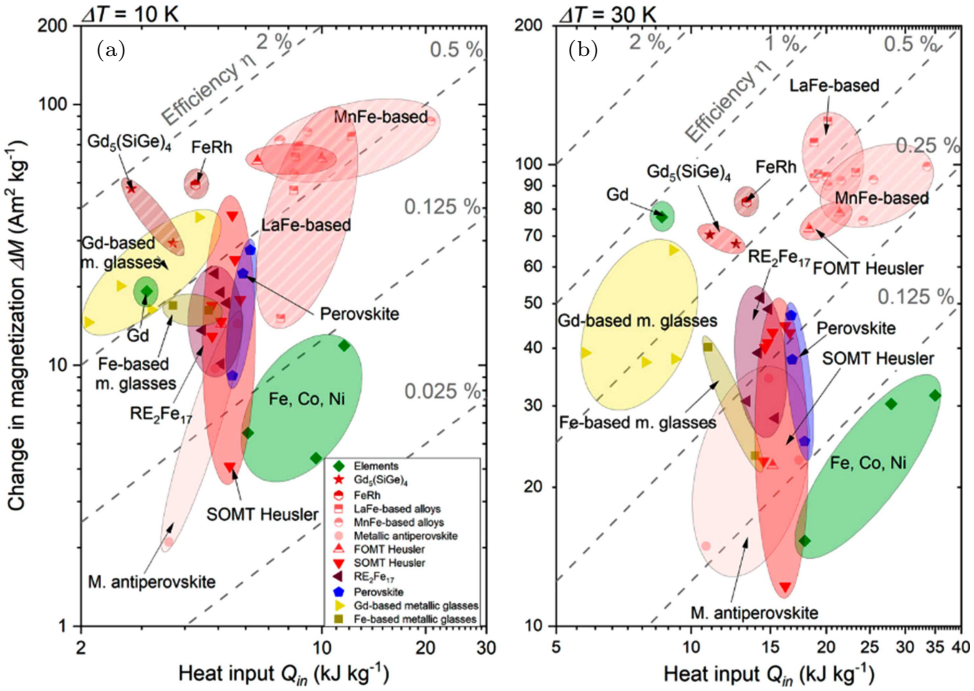



**Fig. 5.** Thermodynamic efficiency ($\eta$) of TMG materials at (a) $\Delta T = 10$ K, and (b) $\Delta T = 30$ K. Metallic materials are displayed in shades of red, ceramics in blue, metallic glasses in shades of yellow, and elements in green.[35]

## 4. Active TMG devices

### 4.1. Active TMG devices with traditional magnetic circuits

Figure 6(a) illustrates the working mechanism of an active TMG device. At low temperatures, the TMG material exhibits high magnetization, which enables magnetic flux ($\Phi$) to flow through a closed magnetic circuit. When the temperature rises, the magnetization of TMG material decreases, thereby opening the magnetic circuit and reducing the magnetic flux. According to Faraday's law, this change in flux induces an electrical voltage. To harvest the resulting electrical energy, an induction coil is wound around a soft magnetic yoke that links the permanent magnet to the TMG material. The repeated opening

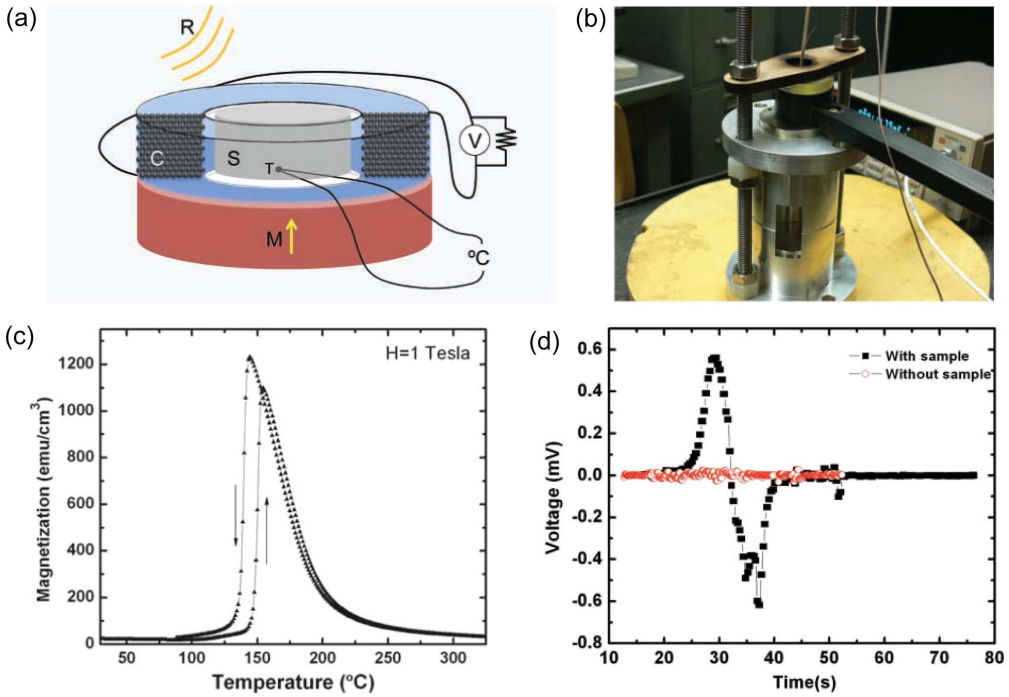



**Fig. 6.** Schematic (a) and actual (b) views of the demonstration. (c) The $M$–$T$ curve under 1 T field for $Ni_{45}Co_5Mn_{40}Sn_{10}$. (d) Measurement of voltage vs. time.[34]

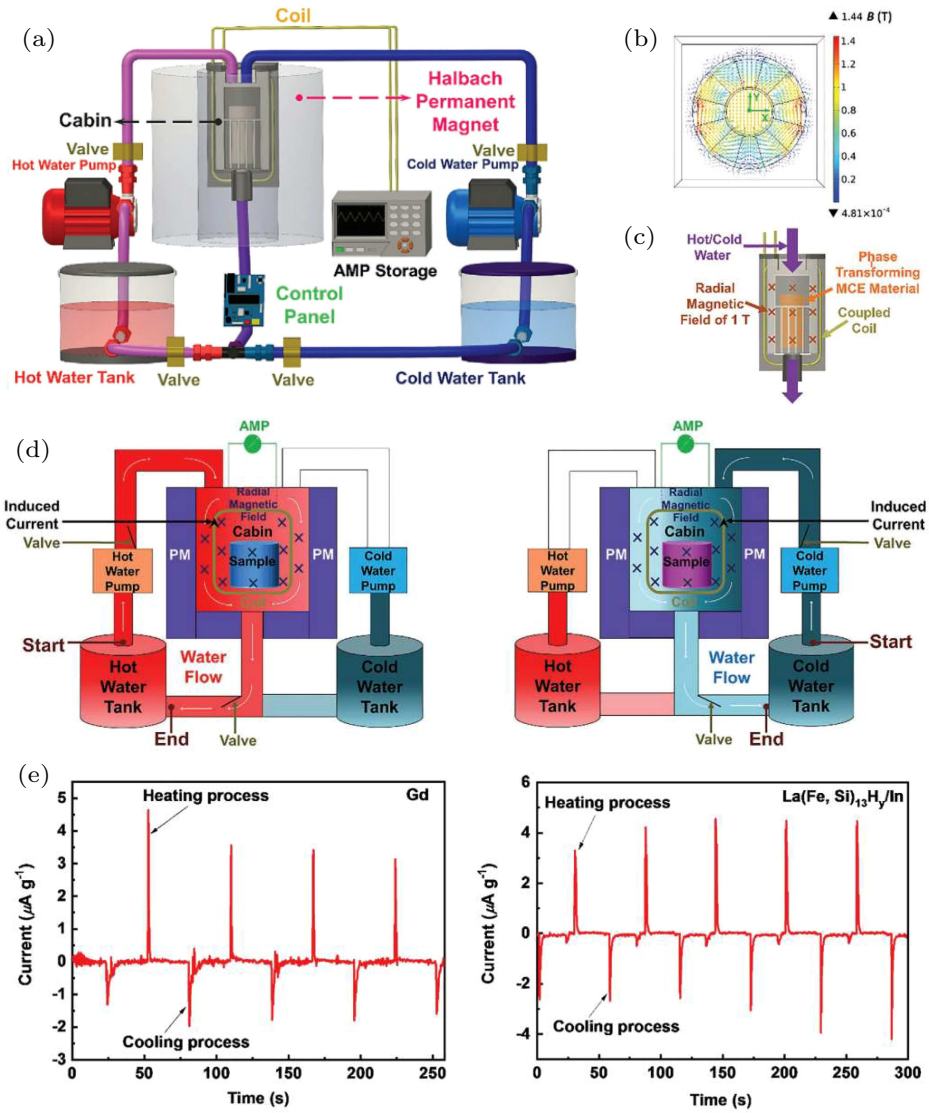



**Fig. 7.** (a) Schematic diagram of the TMG device. (b) The distribution of the radial magnetic field provided by the Halbach permanent magnet. (c) The detailed structure of the 3D printed sample storehouse. (d) The working mechanism of the TMG device. (e) Experimental induced current as a function of time for Gd and La(Fe, Si)$_{13}$H$_y$/In composite.[49]

and closing of the magnetic circuit not only generates voltage but also alters the magnetic field acting on the TMG material itself. In 2011, Srivastava *et al.*[34] investigated an active TMG device based on a multiferroic Heusler alloy; the prototype of their lab-built active TMG device is shown in Fig. 6(b). Figure 6(c) shows the *M*–*T* curve under 1 T for the working material. $Ni_{45}Co_5Mn_{40}Sn_{10}$ undergoes a FOMT from a strongly FM austenite phase to a weakly FM martensite phase at a critical temperature of 408 K, in contrast to Gd, which exhibits an SOMT from an FM to PM state. The thermal energy required at the transition temperature for a FOMT is dominated by latent heat, while SOMT primarily involves sensible heat. As a result, Heusler alloys typically demand a higher heat input per thermomagnetic cycle than Gd.

In their experiment, the Heusler alloy was heated from 75 °C to 375 °C within 30 s using a heat gun. Figure 6(d) shows the *V*–*t* curve during one cycle. Under an applied magnetic field of 0.2 T, the device generated a peak voltage of only 0.6 mV from a 2000-turn induction coil. The predicted conversion efficiency under a 10 °C temperature span (with a hot end temperature of 27 °C) was just 0.004%. This low efficiency was primarily attributed to the non-optimized magnetic circuit. The authors concluded that although the overall efficiency was limited, the material may still be suitable for energy conversion in low-temperature-gradient conditions, where efficiency is not the sole or most appropriate performance metric.

In 2021, Ma *et al.*[49] developed another active TMG device, as shown in Fig. 7(a), in which a 1 T magnetic field was generated using a cylindrical Halbach permanent magnet (Fig. 7(b)). Figure 7(c) shows the detailed structure of the 3D printed sample storehouse. A cylindrical sample was placed in a nylon compartment surrounded by a 300-turn copper coil. Ice water (∼ 273 K) and boiling water (∼ 373 K) served as the cold and hot sources, respectively, providing a working temperature range of 288–353 K, which is well suited for low-grade heat recovery.

Figure 7(d) shows the working mechanism during heating and cooling processes. A programmed microcontroller alternately directs hot and cold water through the sample chamber. When hot water flows through, the TMG material is heated above its $T_C$, undergoing a phase transition from the FM to the PM state. This change alters the magnetic flux through the surrounding coil, inducing an electrical current according to Faraday's law. Conversely, when cold water is introduced, the material transitions back to the FM state, reversing the change in magnetic flux and thus generating a current in the opposite direction. Figure 7(e) shows the $V$–$t$ curves for Gd and La(Fe, Si)$_{13}$H$_y$/In composite. Alternating positive and negative currents are produced through cyclic thermally induced magnetic transitions. In experimental tests, the TMG device using the classic benchmark material Gd produced a relatively low power density of 0.1 mW·m$^{-3}$. For comparison, a similar device based on the La(Fe, Si)$_{13}$H$_y$/In material achieved a power density of 0.42 mW·m$^{-3}$ under the same conditions, highlighting the superior performance of the La(Fe, Si)$_{13}$H$_y$-based system.

To further enhance the performance of Ma *et al.*'s TMG device, Liu *et al.*[42] systematically investigated the influence of key material and device parameters on TMG performance through finite element simulations. Figure 8(a) shows the relationship between the induced current ($I$) peak and the reduction ratio of the cross-sectional area ($S$) as a function of the sample cabin height. The trend of $I$ closely follows that of $S$, confirming that reducing the cabin size enhances TMG performance. Figure 8(b) shows the peak $I$ value as a function of $T_{hot}$ and $T_{cold}$. The maximum current is obtained when $T_{hot}$ is highest and $T_{cold}$ is lowest, while the minimum occurs under the opposite conditions. This indicates that a wider operating temperature range is beneficial for improving TMG output. Figure 8(c) summarizes the sensitivity of the peak $I$ value to variations in several key parameters. Among them, cabin size has the most significant effect: a 100% change in cabin size leads to more than a 20% increase in the peak current. Additionally, the peak current remains nearly constant as the cycle period decreases, up to a limit of 10 s. Therefore, a cycle period of 10 s was selected to enable more frequent current peaks. Figure 8(d) compares the simulated $I$–$t$ curves before and after optimization. After optimizing the device parameters, the simulated peak current during the heating process increased significantly from 28.8 μA to 136.1 μA, while the cooling peak rose from −12.2 μA to −65.0 μA. These results clearly demonstrate that proper optimization of structural and operational parameters can significantly enhance the performance of TMG devices.

Building on the optimized TMG device parameters, Chen *et al.*[44] developed a new-generation active TMG device featuring a more compact sample cabin. Figure 9(a) shows the detailed structure of the lab-built TMG device. A 3D-printed nylon shell was embedded within a hollow permanent magnet (∼ 1 T). The nylon shell is divided into two parts: side A serves as the water inlet, and side B as the outlet. A copper cabin passes through the center of the nylon shell and is wrapped with a 600-turn copper coil. The cold and hot water was pumped to alternatively flow through the copper cabin by a programmable microcontroller, resulting in a reverse FM–PM transition in the material, then an AC current can be continuously obtained in the coil.

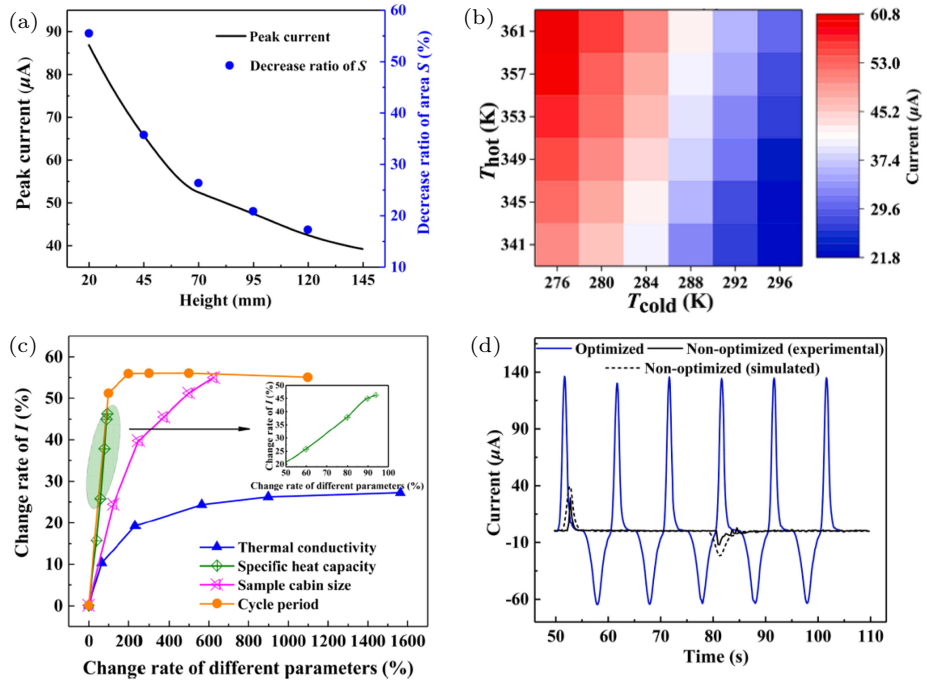



**Fig. 8.** (a) Simulated peak $I$ value and the decrease ratio of area $S$ as a function of the sample cabin height. (b) Simulated peak $I$ value as a function of $T_{hot}$ and $T_{cold}$. (c) The change rate of peak $I$ value as a function of the change rate of different parameters. (d) Comparison of the simulated $I$–$t$ curves before and after optimization.[42]

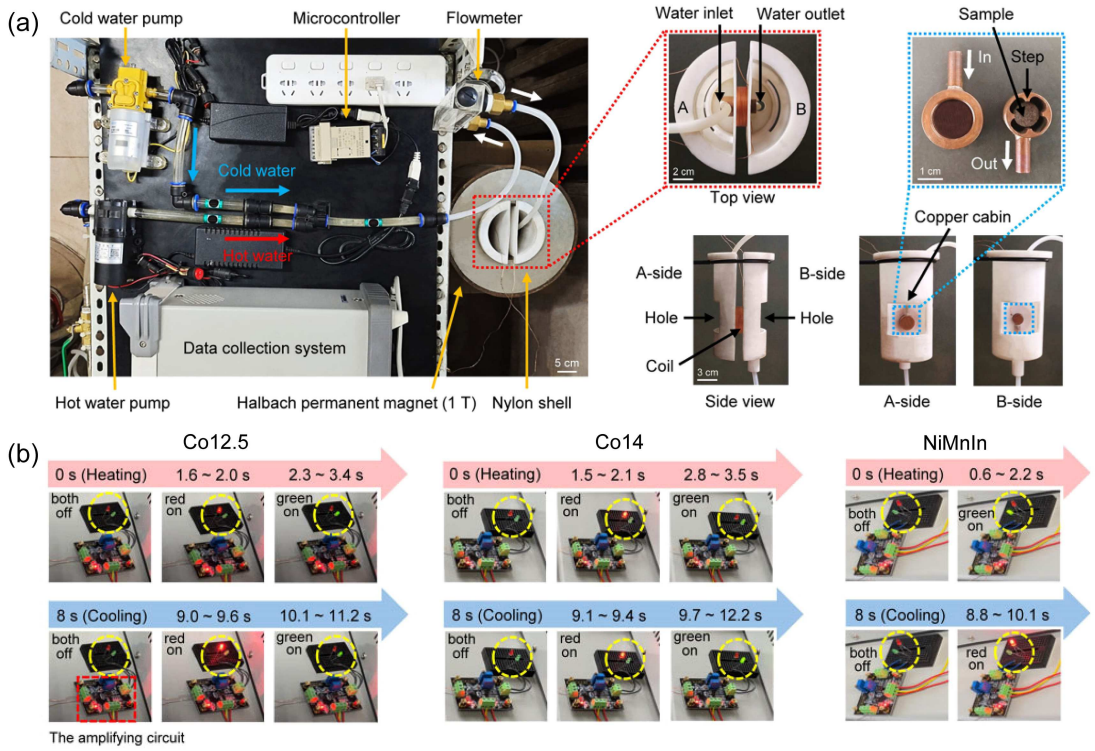



**Fig. 9.** (a) Photograph of the lab-built TMG device, showing the detailed structure of nylon shell and copper cabin. (b) Time dependence of the OFF and ON states of the LEDs for Co12.5, Co14, and NiMnIn alloys.[44]

Furthermore, the device was employed to power two LEDs via an amplification circuit using the $Ni_{37.5}Co_{12.5}Mn_{35}Ti_{15}$ (Co12.5), $Ni_{36}Co_{14}Mn_{35.7}Ti_{14.3}$ (Co14), and $Ni_2Mn_{1.4}In_{0.6}$ (NiMnIn) alloys, as shown in Fig. 9(b). Two LEDs oriented in opposite directions were connected in parallel at the output of the amplifier, with the red and green LEDs activated by positive and negative voltages, respectively. Due to the successive opposite voltage signals generated by the FOMT and SOMT during each heating/cooling cycle in the Co12.5 and Co14 alloys, the red LED lit first, followed by the green one. The brightness of the LEDs corresponded to the magnitude of the induced voltage (see Fig. 3(b)), while the illumination duration matched the width of the voltage peaks. Notably, the NiMnIn alloy, which exhibits a SOMT, produced relatively high and broad voltage peaks. As a result, the LEDs powered by NiMnIn appeared brighter and remained lit significantly longer than those powered by Co12.5 and Co14 alloys, further confirming its superior TMG performance.

### 4.2. Active TMG devices with topological magnetic circuit

In 2018, Waske *et al.*[32] proposed an active TMG device featuring a pretzel-like magnetic flux topology, as shown in Fig. 10(a), employing La–Fe–Co–Si as the working material due to its low magnetic hysteresis. Figure 10(b) shows the topologies of magnetic circuits of TMGs for different genera. Unlike conventional magnetic circuits (Genus = 1 or 2), where the magnetic flux within the induction coil varies between zero and a maximum value, Waske *et al.*'s design (Genus = 3) enables the flux to oscillate between negative and positive maxima. At an operating frequency of 0.8 Hz and a temperature variation of 23 °C, the device achieved a peak power output of 1.24 mW. Experimental comparisons with traditional magnetic circuit configurations showed that this novel topology improved both voltage and power output by up to two orders of magnitude.[60,61]

Recently, Liu *et al.*[43] designed a TMG device optimized for low-temperature waste heat recovery, as shown in Fig. 10(c). In this configuration, temperature-sensitive FM–PM transitions in TMG materials, such as Gd plates or La(Fe, $Si)_{13}H_y$/In composites, act as a thermal switch to control the magnetic circuit's ON/OFF state. The improved integration enables the magnetic flux within the coil to swing between positive and negative maxima, significantly enhancing the induced voltage, which ranges from 0.04 V to 0.19 V. This design also reduces magnetic stray fields and minimizes the quantity of rare-earth material used, thus lowering the economic cost of the device. The authors demonstrated the system's functionality by successfully lighting an LED (Fig. 10(d)), suggesting that an array of such TMG modules could effectively convert low-grade waste heat into electricity.

Furthermore, Bahl *et al.*[62] optimized Liu *et al.*'s design to further increase magnetic flux variation and improve output performance. Figure 10(e) shows the prototype realized with a small coil, their optimized device utilized 126 g of Gd spheres in the sample chamber. At a temperature span of

40 °C and a hot-side temperature of 40 °C, the device delivered a power output of 9 mW at a flow rate of 1.4 L·min$^{-1}$ (Fig. 10(f)). When normalized by material volume and temperature span, the resulting power density $(P/(V\Delta T))$ was 0.0058 mW·cm$^{-3}$·K$^{-1}$. Although this value is lower than that of Liu *et al.*'s device, the discrepancy is primarily attributed to the choice of working material. Liu *et al.*'s device employed LaFeSi-based composites, which have demonstrated power outputs nearly an order of magnitude higher than those using Gd. Therefore, it is anticipated that replacing Gd with LaFeSi in Bahl *et al.*'s configuration could significantly enhance the power density of the system.

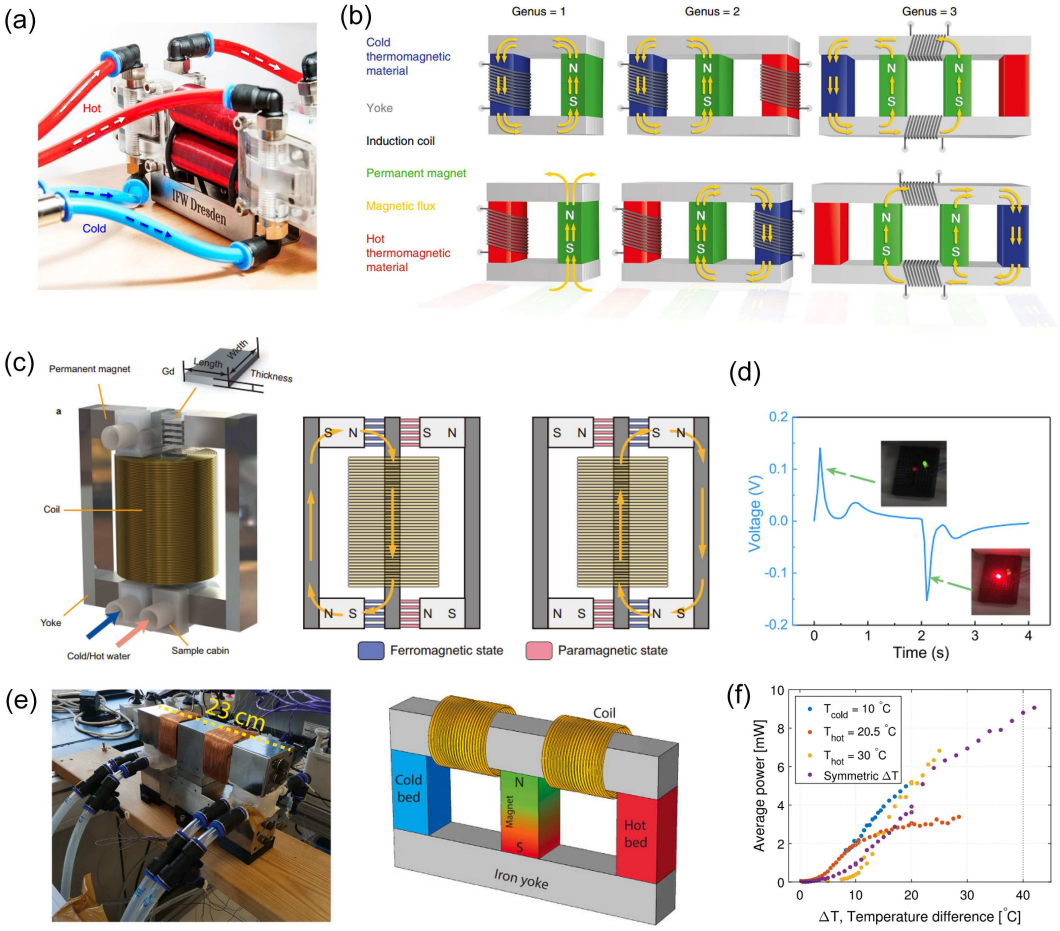



**Fig. 10.** (a) Photo of the TMG device. (b) Topologies of magnetic circuits of TMGs for different genera.[32] (c) Magnetic circuit structure design and working principle of the TMG device. (d) Utilize devices to light up LEDs. (e) The experimental prototype realized with the small coils.[43] (f) The average power as a function of temperature difference between $T_{hot}$ and $T_{cold}$.[62]

## 5. Passive TMG devices

### 5.1. Thermomagnetic oscillators

In 2007, Ujihara *et al.*[63] fabricated one of the earliest TMG harvesters by attaching a piezoelectric spring to a soft magnetic element. The conceptual design and working mechanism are illustrated in Figs. 11(a) and 11(b). In this device, a soft ferromagnetic material (Gd) is suspended on a serpentine spring near a permanent magnet. Initially, when Gd is below its $T_C$, it is attracted to the magnet. As it heats above $T_C$, it becomes paramagnetic and is repelled by the spring toward the heat sink. Once cooled below $T_C$, Gd regains its magnetism and is again pulled toward the magnet. This cycle repeats, producing sustained mechanical oscillations driven by the SOMT. Usually, the resulting mechanical energy can then be converted into electrical energy using a coil,[64–66] and even piezoelectric[67–69] or triboelectric[70–73] transduction mechanisms. In this work, the resulting motion generates electrical power via piezoelectric conversion. Figure 11(c) shows the power density as a function of gap for active Gd element. With a spatial temperature difference between 50 °C (hot side) and 0 °C (cold side), and a gap of 0.2 mm, the device achieved a power density of 3.5 mW·cm$^{-2}$.

In 2016, Gueltig *et al.*[41] developed a high-performance passive TMG device based on Ni–Mn–Ga Heusler alloy films. The device photo and operating principle are shown in Figs. 11(d) and 11(e). In the FM state, the cantilever deflects toward the heated magnet, where it undergoes a magnetic phase transition. In the PM state, the elastic restoring force dominates and resets the cantilever position. This competition between magnetic and elastic forces induces self-sustained periodic motion, converting thermal energy into mechanical work, and subsequently into electrical energy via in-

duction in a pickup coil. Figure 11(f) shows the time-resolved experimental characteristics of displacement of the center-of-mass and corresponding electrical current induced in the pick-up coil. Using a 220 Ω load, peak currents of approximately ±180 μA were observed as the cantilever approached and retreated from the magnet. The system demonstrated an average power density of 118 mW·cm$^{-3}$, comparable to that of some TEGs. Moreover, it required a minimal temperature fluctuation of just 3 K, and each thermomagnetic cycle lasted only ∼ 12 ms, aligning well with the oscillation period.

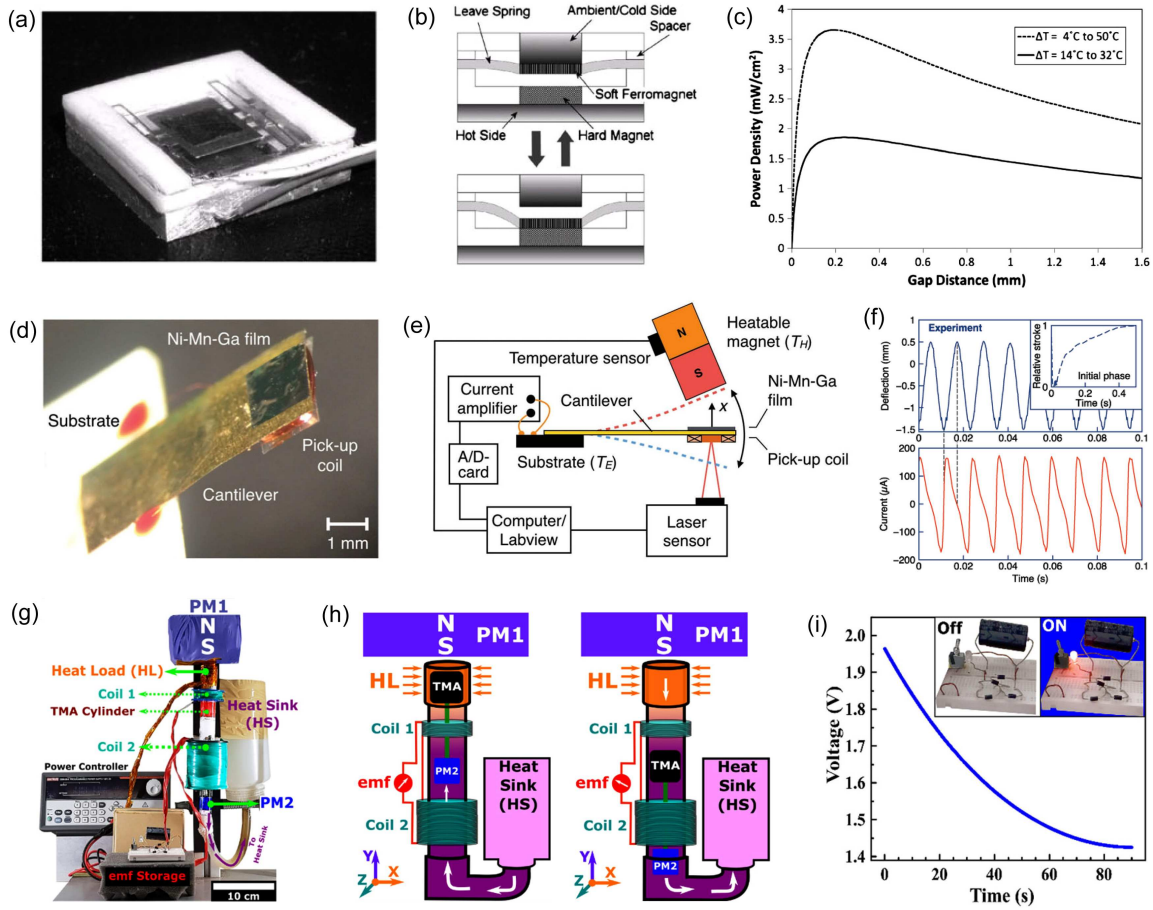



**Fig. 11.** (a) Actual device and (b) cross section during cooling and heating. (c) Power density as a function of gap for active Gd element.[63] (d) Actual device and (e) operation principle of the TMG device. (f) Time-resolved experimental characteristics of displacement of the center-of-mass and corresponding electrical current induced in the pick-up coil.[41] (g) Experimental device and (h) schematic of up and down positions of the hybrid thermomagnetic oscillator (HTMO). (i) The capacitor voltage discharge across the LED.[14]

In 2019, Deepak *et al.*[14,33] introduced a hybrid thermomagnetic oscillator (HTMO) capable of both heat-load cooling and electricity harvesting. The TMG material used was a bulk alloy with the composition $(MnNiSi)_{0.7}(Fe_2Ge)_{0.3}$ and a $T_C$ of 144 °C. The photo and working principle of the HTMO are illustrated in Figs. 11(g) and 11(h). The device was constructed by mechanically connecting an NdFeB permanent magnet to the TMG material via a spacer. During oscillation, voltage was induced in two copper solenoid coils placed in series (coils 1 and 2), with contributions from both the TMG material and the magnet. The system achieved up to 10 V per cycle and a peak current of 15 mA. Figure 11(i) shows the capacitor voltage discharge across the LED. They used the stored energy to light up an LED which is connected to the capacitor by a switch. The stored energy continuously discharges across the LED, lighting it for 90 s, demonstrating the potential of HTMO devices for combined thermal management and energy harvesting.

### 5.2. Thermomagnetic motors

Thermomagnetic motors (also referred to as Curie wheels) convert thermal energy into mechanical rotation by exploiting the temperature-dependent magnetization of ferromagnetic materials. Early concepts of such devices were proposed by Edison[24] and Tesla,[23] and subsequent theoretical studies have suggested that their efficiency could approach the thermodynamic limit.

Ahmed *et al.*[74] demonstrated a hybrid system by combining a thermomagnetic engine with a rotary triboelectric and electromagnetic generator. Figure 12(a) shows the schematic of the motor. Their hybrid energy harvester consists of a thermomagnetic engine mechanically coupled to both a triboelectric generator and an electromagnetic generator. Figure 12(b) shows the fabrication process of the triboelectric generator. The triboelectric component was fabricated using

internal acrylic and external aluminum interdigital electrodes. Alternating current was generated as the acrylic plate moved across the electrodes due to rotation. Figure 12(c) shows the rotation speed as a function of temperature difference. The maximum rotational speed of the shaft reached 263 rpm depending on the hot water temperature. The corresponding open-circuit voltage and short-circuit current values reached 15.6 V and 9.82 μA, respectively (Fig. 12(d)), with a maximum output power of 14.4 μW (Fig. 12(e)).

More recently, as shown in Fig. 12(f), Cugini *et al.*[75] developed a compact thermomagnetic motor prototype designed as a flexible test-bench to evaluate and compare the thermomagnetic performance of small quantities ($< 0.3$ g) of new materials under variable conditions. Three representative Ni–Mn-based Heusler alloys, including NiMnIn, NiMnSn, and NiMnCuGa, were mechanically processed into disk-shaped wheels and tested in the prototype device. Figure 12(g) shows the rotors made of NiMnIn with a radial thickness of 1 mm and 1.5 mm. The mechanical power output generated by the motor was closely correlated with the magnetic properties of the materials, particularly the magnetic transition temperature and saturation magnetization, which strongly influence the energy conversion efficiency. Figure 12(h) shows the maximum mechanical power output as a function of temperature of the warm reservoir. Among the tested alloys, NiMnIn achieved the highest mechanical output power, reaching $0.70 \pm 0.04$ mW when normalized by the mass or volume of active material. This work underscores the importance of material selection and magnetic transition behavior in the development of efficient thermomagnetic energy conversion systems.

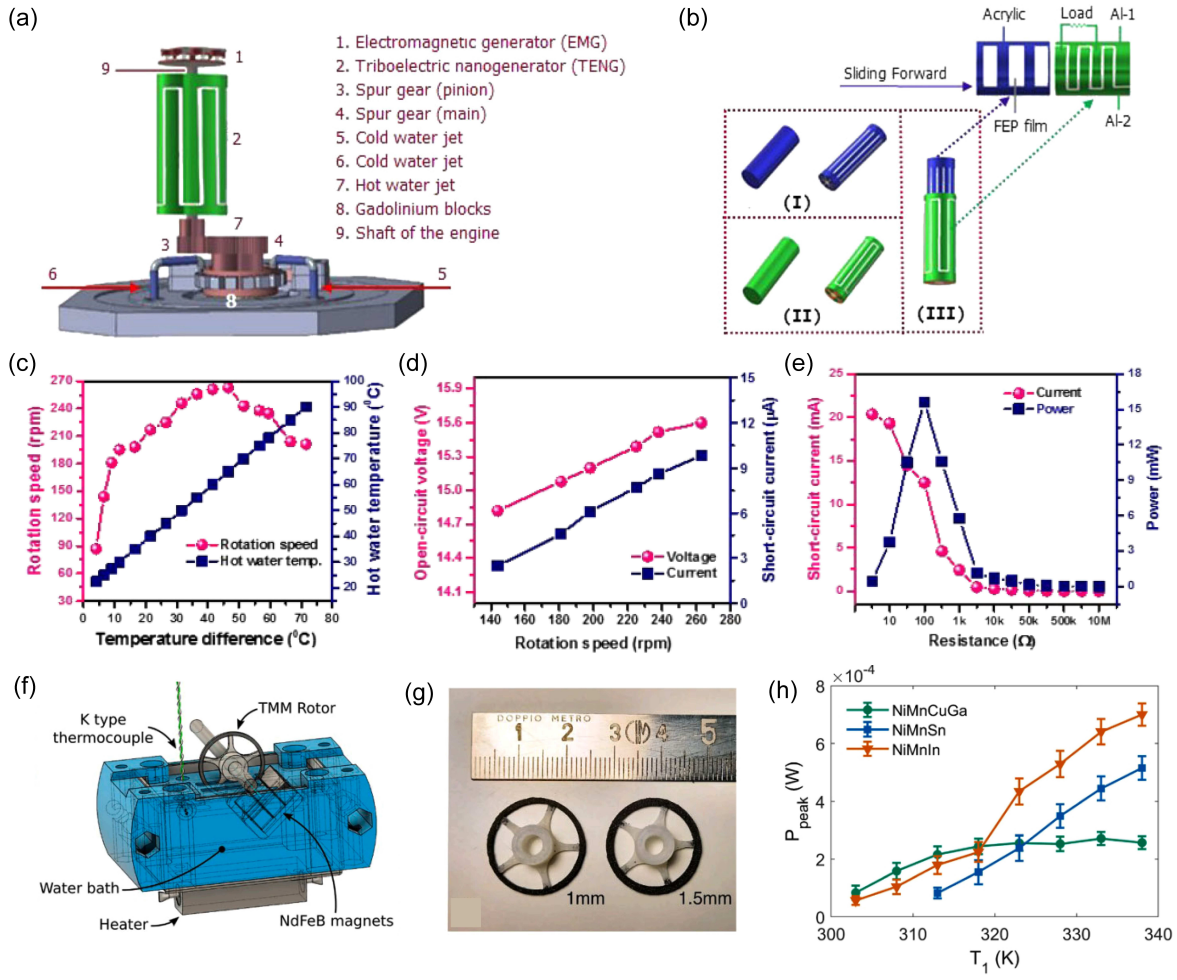



**Fig. 12.** (a) Schematic of the thermomagnetic generator. (b) Schematic diagram illustrating the fabrication process of the triboelectric generator. (c) Temperature difference vs. rotation speed. (d) Open-circuit voltage and short-circuit current of the TENG on different rotation speeds. (e) The power output of the TENG at different loads.[74] (f) Technical scheme of the small-scale TM motor prototype utilized for testing materials. (g) Rotors made of NiMnIn with a radial thickness of 1 mm and 1.5 mm. (h) Maximum mechanical power output as a function of temperature of the warm reservoir for a ring of NiMnIn (orange triangles), NiMnSn (blue squares) and NiMnCuGa (green circles).[75]

## 6. Conclusion and outlook

In this review, we summarized recent advances in TMG from both materials and device perspectives. Various TMG materials, including rare-earth-based compounds, Heusler alloys, and LaFe-based alloys, have been investigated for their potential in low-grade heat harvesting. Among them, SOMT materials with high thermal conductivity and zero hysteresis

show particular promise. On the device level, both active and passive configurations have been developed, with ongoing efforts focused on enhancing flux control, thermal management, and integration efficiency. Hybrid systems combining TMG with triboelectric or piezoelectric mechanisms further broaden the application potential of this technology.

Despite recent advances, several key challenges must be addressed before TMG technologies can be widely deployed. First, most existing materials suffer from thermal hysteresis, low magnetization, or poor thermal conductivity, which limits its efficiency and stability under cyclic operation. The development of new TMG materials with sharp, reversible phase transitions, tunable Curie temperatures, and high thermal conductivity is essential. Second, efficient thermal management remains a bottleneck, requiring better thermal interfaces and faster heat transfer mechanisms to enhance temperature gradients and improve energy conversion rates. Third, current device architectures are often difficult to scale due to complex magnetic circuits and heating setups. Future efforts should focus on designing compact, modular, and low-cost TMG systems that integrate high-performance materials with optimized magnetic and thermal pathways.

Looking forward, it is also important to establish quantitative performance targets to guide material and device design. For instance, achieving an average power density above 100 $\mathrm{mW{\cdot}cm^{-3}}$ and a thermal-to-electric conversion efficiency greater than 5% would make TMG competitive with thermoelectric generators in low-grade waste heat recovery. In addition, ensuring operational stability beyond $10^6$ heating/cooling cycles without performance degradation and reducing material costs to levels comparable with current thermoelectrics are essential for practical adoption.

Moreover, integrating TMG with hybrid harvesting techniques, such as triboelectric, piezoelectric, or thermoelectric methods, could expand functionality and improve overall energy output. Long-term stability, material cost, and environmental compatibility must also be considered to ensure practical viability. Looking ahead, the combination of advanced material discovery, computational modeling, and system-level engineering will accelerate progress in the field. With continued interdisciplinary development, TMG holds great promise for applications in low-grade waste heat recovery, self-powered sensing, wearable electronics, and distributed energy systems. Typical low-power applications illustrate this potential: 0.1 μW for a 32 kHz quartz oscillator, 1 μW for an electronic watch or calculator, 10 μW for pressure or temperature sensors, 50 μW for short-range RF emission, 100 μW for implanted medical devices, and about 500 μW for hearing aid LCD displays. In particular, the power output achievable with optimized TMG devices could meet the demands of many of these applications, contributing to the broader goals of sustainable and decentralized energy conversion.

## Acknowledgements

This work was supported by the National Natural Science Foundation of China (Grant Nos. 52171169 and 52101210), the National Key Research and Development Program of China (Grant No. 2021YFB3501204), the State Key Laboratory for Advanced Metals and Materials (Grant No. 2023-ZD01), USTB Concept Verification Funding Project (Grant No. GNYZ-2024-6), Fundamental Research Funds for the Central Universities (Grant No. FRF-TP-24-004A), USTB Research Center for International People-to-people Exchange in Science, Technology and Civilization (Grant Nos. 2024KFZD001 and 2024KFYB004).

## References

[1] Forman C, Muritala I K, Pardemann R and Meyer B 2016 *Renewable Sustainable Energy Rev.* **57** 1568
[2] Schierning G 2018 *Nat. Energy* **3** 92
[3] Kishore R A and Priya S 2017 *Sustain. Energy Fuels* **1** 1899
[4] Madhawa Hettiarachchi H D, Golubovic M, Worek W M and Ikegami Y 2007 *Energy* **32** 1698
[5] Firth A, Zhang B and Yang A D 2019 *Appl. Energy* **235** 1314
[6] Chen L, Msigwa G, Yang M Y, Osman A I, Fawzy S, Rooney D W and Yap P S 2022 *Environ. Chem. Lett.* **20** 2277
[7] Kim T Y, Kwak J and Kim B W 2018 *Energy Convers. Manage.* **160** 14
[8] Choi J, Cho K, Yun J, Park Y, Yang S and Kim S 2017 *Adv. Energy Mater.* **7** 1700972
[9] Radouane N 2023 *Chin. Phys. B* **32** 057307
[10] Bucsek A, Nunn W, Jalan B and James R D 2019 *Phys. Rev. Appl.* **12** 034043
[11] Zhao T T, Jiang W T, Niu D, Liu H Z, Chen B D, Shi Y S, Yin L and Lu B H 2017 *Appl. Energy* **195** 754
[12] Ravindran S K T, Huesgen T, Kroener M and Woias P 2011 *Appl. Phys. Lett.* **99** 104102
[13] Ren J 2023 *Chin. Phys. Lett.* **40** 090501
[14] Deepak K, Varma V B, Prasanna G and Ramanujan R V 2019 *Appl. Energy* **233–234** 312
[15] Kishore R A, Davis B, Greathouse J, Hannon A, Emery Kennedy D, Millar A, Mittel D, Nozariasbmarz A, Kang M G, Kang H B, Sanghadasa M and Priya S 2019 *Energy Environ. Sci.* **12** 1008
[16] Hur S, Kim S, Kim H S, Kumar A, Kwon C, Shin J, Kang H, Sung T H, Ryu J, Baik J M and Song H C 2023 *Nano Energy* **114** 108596
[17] Kishore R A and Priya S 2018 *Materials* **11** 1081433
[18] Vuarnoz D, Kitanovski A, Gonin C, Borgeaud Y, Delessert M, Meinen M and Egolf P W 2012 *Appl. Energy* **100** 229
[19] Chiolerio A, Garofalo E, Mattiussi F, Crepaldi M, Fortunato G and Iovieno M 2020 *Appl. Energy* **277** 115591
[20] Bevione M, Garofalo E, Cecchini L and Chiolerio A 2020 *MRS Energy Sustain.* **7** 1
[21] Cai C C, Luo B, Liu Y H, Fu Q, Liu T, Wang S F and Nie S X 2022 *Mater. Today* **52** 299
[22] Chatterjee S, Burman S R, Khan I, Saha S, Choi D, Lee S and Lin Z-H 2020 *Nanoscale* **12** 17663
[23] Tesla N (U.S. Patent) 428,057 [1890]
[24] Edison (U.S. Patent) 476,983 [1892]
[25] Elliott J F 1959 *J. Appl. Phys.* **30** 1774
[26] Stauss H E 1959 *J. Appl. Phys.* **30** 698
[27] Kirol L D and Mills J I 1984 *J. Appl. Phys.* **56** 824
[28] Tegus O, Brück E, Buschow K and Boer F 2002 *Nature* **415** 150
[29] Moya X, Kar-Narayan S and Mathur N D 2014 *Nat. Mater.* **13** 439
[30] Smith A, Bahl C R H, Bjørk R, Engelbrecht K, Nielsen K K and Pryds N 2012 *Adv. Energy Mater.* **2** 1288
[31] Chen H D, Ma Z H, Liu X L, Qiao K M, Xie L L, Li Z X, Shen J, Dai W, Ou Z Q, Yibole H, Tegus O, Taskaev S V, Chu K, Long Y and Zhang H 2022 *Appl. Energy* **306** 117999

[32] Waske A, Dzekan D, Sellschopp K, Berger D, Stork A, Nielsch K and Fähler S 2018 *Nat. Energy* **4** 68

[33] Deepak K, Pattanaik M S and Ramanujan R V 2019 *Appl. Energy* **256** 113917

[34] Srivastava V, Song Y, Bhatti K and James R D 2011 *Adv. Energy Mater.* **1** 97

[35] Dzekan D, Waske A, Nielsch K and Fähler S 2021 *APL Mater.* **9** 011105

[36] Song Y T, Bhatti K P, Srivastava V, Leighton C and James R D 2013 *Energy Environ. Sci.* **6** 1315

[37] Zabek D and Morini F 2019 *Therm. Sci. Eng. Prog.* **9** 235

[38] Rashidi S, Ehsani M H, Shakouri M and Karimi N 2021 *J. Magn. Magn. Mater.* **537** 168112

[39] Kishore R A and Priya S 2018 *Renewable Sustainable Energy Rev.* **81** 34

[40] Solomon D 1988 *J. Appl. Phys.* **63** 915

[41] Gueltig M, Wendler F, Ossmer H, Ohtsuka M, Miki H, Takagi T and Kohl M 2017 *Adv. Energy Mater.* **7** 1601879

[42] Liu X L, Zhang H, Chen H D, Ma Z H, Qiao K M, Xie L L, Ou Z Q, Wang J, Hu F X and Shen B G 2023 *Appl. Therm. Eng.* **221** 119827

[43] Liu X L, Chen H D, Huang J Y, Qiao K M, Yu Z Y, Xie L L, Ramanujan R V, Hu F X, Chu K, Long Y and Zhang H 2023 *Nat. Commun.* **14** 4811

[44] Chen H D, Liu M Z, Yu Z Y, Qiao K M, Naeem M Z, Liu J Y, Xie L L, Liu Y, Huang M F, Li Z X, Shen J, Hu F X, Shen B G and Zhang H 2025 *Adv. Mater.* **37** 2500544

[45] Chen H D, Liu X L, Liu Y, Xie L L, Yu Z Y, Qiao K M, Liu M Z, Hu F X, Shen B G, Ramanujan R V, Chu K and Zhang H 2024 *Mater. Horiz.* **11** 2603

[46] Jiang C, Zhu S M, Yu G Y, Luo E C and Li K 2022 *Appl. Energy* **311** 118585

[47] Joseph J, Fontana E, Devillers T, Dempsey N M and Kohl M 2023 *Adv. Funct. Mater.* **33** 2301250

[48] Kishore R A, Singh D, Sriramdas R, Garcia A J, Sanghadasa M and Priya S 2020 *J. Appl. Phys.* **127** 044501

[49] Ma Z H, Chen H D, Liu X L, Xing C F, Wu M L, Wang Y X, Liu P R, Ou Z Q, Shen J, Taskaev S V, Long K W, Long Y and Zhang H 2021 *Adv. Sustainable Syst.* **5** 2000234

[50] Song Y 2014 *Phys. Chem. Chem. Phys.* **16** 12750

[51] Post A, Knight C and Kisi E 2013 *J. Appl. Phys.* **114** 033915

[52] Pecharsky A O, Gschneidner K A and Pecharsky V K 2003 *J. Appl. Phys.* **93** 4722

[53] Raj Kumar D M, Manivel Raja M, Prabahar K, Chandrasekaran V, Poddar A, Ranganathan R and Suresh K G 2011 *J. Magn. Magn. Mater.* **323** 1750

[54] Christiaanse T and Brück E 2014 *Metall. Mater. Trans. E* **1** 36

[55] Bi L G, Tegus O, Yi R Shi H R 2012 *Acta Phys. Sin.* **61** 077103 (in Chinese)

[56] Liu Z S, Tegus O, Ou Z Q, Fan W D, Song Z Q, Ha Si Chao Lu, Wei W and Han R 2015 *Acta Phys. Sin.* **64** 047103 (in Chinese)

[57] Liu J Q, Long Y, Bai D L, Sun H, Zhang H, Long K W and Yan T B 2019 *AIP Adv.* **9** 045227

[58] Lallart M, Wang L, Sebald G, Petit L and Guyomar D 2014 *Phys. Lett. A* **378** 3151

[59] Ahmim S, Almanza M, Loyau V, Mazaleyrat F, Pasko A, Parrain F and LoBue M 2021 *J. Magn. Magn. Mater.* **540** 168428

[60] Dzekan D, Kischnik T D, Diestel A, Nielsch K and Fähler S 2022 *J. Phys.: Energy* **4** 024006

[61] Dzekan D, Diestel A, Berger D, Nielsch K and Fahler S 2021 *Sci. Technol. Adv. Mater.* **22** 643

[62] Bahl C R H, Engelbrecht K, Gideon A, Levy M A V, Marcussen J B, Imbaquingo C and Bjørk R 2024 *Appl. Energy* **376** 124304

[63] Ujihara M, Carman G P and Lee D G 2007 *Appl. Phys. Lett.* **91** 093508

[64] Gueltig M, Ossmer H, Ohtsuka M, Miki H, Tsuchiya K, Takagi T and Kohl M 2014 *Adv. Energy Mater.* **4** 1400751

[65] Joseph J, Ohtsuka M, Miki H and Kohl M 2022 *iScience* **25** 104569

[66] Joseph J, Ohtsuka M, Miki H and Kohl M 2020 *Joule* **4** 2718

[67] Chen C, Chung T, Tseng C, Hung C, Yeh P and Cheng C 2015 *IEEE Trans. Magn.* **51** 9100309

[68] Chun J, Song H C, Kang M G, Kang H B, Kishore R A and Priya S 2017 *Sci. Rep.* **7** 41383

[69] Chun J, Kishore R A, Kumar P, Kang M G, Kang H B, Sanghadasa M and Priya S 2018 *ACS Appl. Mater. Interfaces* **10** 10796

[70] Rodrigues C, Pires A, Gonçalves I, Silva D, Oiiveira J, Pereira A and Ventura J 2022 *Adv. Funct. Mater.* **32** 2110288

[71] Gong S K, Wang X W, Tang B Z, Xiong Z Y, Qi S, Chen J, Yu P and Guo H Y 2024 *Adv. Mater.* **36** 2402824

[72] Li H, Kim I, Goh T S, Il Lee J and Kim D 2025 *Nano Energy* **138** 110899

[73] Kim J, Yoo J, Seo H, Avila R, Chung G, Shin G, Gwak S, Han Y, Lee J H, Yoon H J and Park Y 2025 *Sci. Adv.* **11** eadu5919

[74] Ahmed R, Kim Y, Mehmood M U, Zeeshan, Shaislamov U and Chun W 2019 *Int. J. Energy Res.* **2** 1

[75] Cugini F, Gallo L, Garulli G, Olivieri D, Trevisi G, Fabbrici S, Albertini F and Solzi M 2025 *Acta Mater.* **288** 120847